

High-order upwind compact scheme and simulation of turbulent premixed V-flame

Qing-Yong Zhu^{1,2,‡} and C. K. Chan^{3,*,†}

¹*School of Mathematics and Computational Science, Zhongshan University, Guangzhou 510275, China*

²*Graduate School of Harbin Institute of Technology, Shenzhen 518055, China*

³*Department of Applied Mathematics, The Hong Kong Polytechnic University, Hung Hom, Kowloon, Hong Kong*

SUMMARY

A high-order accurate upwind compact difference scheme with an optimal control coefficient is developed to track the flame front of a premixed V-flame. In multi-dimensional problems, dispersion effect appears in the form of anisotropy. By means of Fourier analysis of the operators, anisotropic effects of the upwind compact difference schemes are analysed. Based on a level set algorithm with the effect of exothermicity and baroclinicity, the flame front is tracked. The high-order accurate upwind compact scheme is employed to approximate the level set equation. In order to suppress numerical oscillations, the group velocity control technique is used and the upwind compact difference scheme is combined with the random vortex method to simulate the turbulent premixed V-flame. Distributions of velocities and flame brush thickness are obtained by this technique and found to be comparable with experimental measurement. Copyright © 2005 John Wiley & Sons, Ltd.

KEY WORDS: upwind compact difference scheme; premixed turbulent V-flame; random vortex method; level set algorithm

1. INTRODUCTION

In turbulent premixed combustion, vortices with small structures exist and interact with the velocity field. Many aspects of the interaction between fluid turbulence and combustion

*Correspondence to: C. K. Chan, Department of Applied Mathematics, The Hong Kong Polytechnic University, Hung Hom, Kowloon, Hong Kong.

†E-mail: ck.chan@polyu.edu.hk

‡E-mail: qingyongzhu@yahoo.com

Contract/grant sponsor: National Natural Science Foundation of China; contract/grant number: 10102024

Contract/grant sponsor: Research Grant Council of the Hong Kong SAR; contract/grant numbers: PolyU 5246/03E, B-Q653

Received 13 November 2004

Revised 16 April 2005

Accepted 23 April 2005

heat release are still not fully understood due to the complexity of the physical phenomena involved. In recent years, a number of studies have been focused on idealized configurations to aid in the understanding of premixed and non-premixed turbulent combustion. Many numerical methods have been developed to simulate the complex flow fields. However, as most of these methods are low-order accurate schemes, numerical results were generally unsatisfactory due to overdissipation. It is therefore necessary to develop high-order accurate finite difference schemes. With the traditional two-level explicit schemes, at least $(N + 1)$ nodes are needed to achieve N th order accuracy. When N is large, the demand for computational time and storage is enormous. Compact schemes have become popular due to their high-order accuracy and small stencils. Compact schemes are methods where the derivatives are approximated not by polynomial operators but by rational function operators on the discrete solutions. Zhu *et al.* [1] proposed an upwind compact difference scheme with third-order accuracy in smooth regions. In the region, where pressure gradient is large, group velocity of the schemes can be controlled [2] to eliminate numerical oscillations, and such a scheme has been successfully used to simulate three-dimensional complex flow fields.

The study of turbulent flames is one of the most defying areas of engineering sciences due to the complexity of the physical phenomena when coupled with chemical reactions. One of the common flame configurations is the V-shaped flame obtained by introducing a rod in a stream of fully premixed reactants as a flame stabilizer [3–5]. While Cheng *et al.* [6–8] provided some experimental data of the V-flame, complexity of the flow field makes detailed measurements rather difficult. Numerical simulation therefore plays an important role in investigating such flow fields. On the interaction of premixed flames with turbulence, direct numerical simulation (DNS) has been employed to simulate the flow field with low turbulent intensities [9, 10]. Baum *et al.* [11] conducted two-dimensional DNS of H₂–air turbulent premixed flames and showed the effects of turbulence characteristics on the local flame structure. They showed that isolated pockets of unburnt gas are observed on the burnt side. However, DNS has been restricted to low Reynolds number flow.

In V-flame, when reaction rate is high and the reaction zone is correspondingly thin, the flame can be considered to be of zero thickness, separating burnt and unburnt regions with different constant densities and propagates into the fresh mixture at a local curvature-dependent flame speed. Pindera and Talbot [12], Rhee *et al.* [13] and Chan *et al.* [14] adopted the random vortex method [15] to simulate the turbulent V-flame with effects of exothermicity and baroclinicity. More recently, Chan *et al.* [16] investigated the effect of intense turbulence on turbulent premixed V-flame. Numerical results indicated that free-stream turbulence affects turbulence statistics greatly including the conditional and unconditional mean axial and transverse velocities, fluctuation velocities and Reynolds stresses. In their work, the flame front is tracked by a level set equation approximated by an upwind scheme. However, the numerical effect of the difference scheme has not been discussed in their work.

The objective of this paper is to develop a more effective numerical method for simulating premixed V-flame. To track the flame front, an upwind compact difference scheme with a control coefficient is used and the group velocity control technique is employed to prevent nonphysical oscillations. Moreover, in multi-dimensional problems, the effect of numerical errors appears in the form of anisotropy. In order to analyse the anisotropic effect, a multi-dimensional model equation is considered so as to obtain an optimal value of the control coefficient for the upwind compact difference scheme. The present method combined with Runge–Kutta time discretization [17] is used to simulate the turbulent premixed V-flame.

Distributions of mean velocities, fluctuation velocities and flame brush thickness are presented and compared with theoretical as well as experimental measurements.

2. ANALYSIS OF DIFFERENCE SCHEMES

2.1. Symbols of difference operators

Consider the one-dimensional unsteady advection of a scalar u with constant positive velocity a , given by

$$u_t + au_x = 0 \quad (1)$$

The solution with the initial condition $u(x, 0) = u_0(x)$ is $u(x, t) = u_0(x - at)$.

To facilitate discussion, let δ_x denote the approximate operator of the spatial differential operator d/dx so that $\Delta x^{-1} \cdot \delta_x \approx d/dx$. Therefore,

$$v_t + a \cdot \Delta x^{-1} \delta_x v = 0 \quad (2)$$

Given $v(x)$, $x \in R^1$ and a positive parameter $\Delta x > 0$, $E_{\Delta x}$ is defined as a shift operator such that $(E_{\Delta x} v)(x) = v(x + \Delta x)$. The operators δ_x^+ , δ_x^- , δ_x^0 , δ_x^2 are defined as

$$\delta_x^+ := E_{\Delta x} - I, \quad \delta_x^- := I - E_{\Delta x}^{-1}, \quad \delta_x^0 := \frac{1}{2}(\delta_x^+ + \delta_x^-), \quad \delta_x^2 := \delta_x^+ \delta_x^- = \delta_x^- \delta_x^+ \quad (3)$$

where I is an identity operator. The subscript x indicates that the operator is applied in the x direction. Based on Fourier transform, the symbols of the operators δ_x^+ , δ_x^- , δ_x^0 , δ_x^2 are

$$\begin{aligned} \hat{\delta}_x^+ &= \cos \alpha - 1 + i \sin \alpha, & \hat{\delta}_x^- &= 1 - \cos \alpha + i \sin \alpha \\ \hat{\delta}_x^0 &= \frac{1}{2}(\hat{\delta}_x^+ + \hat{\delta}_x^-) = i \sin \alpha, & \hat{\delta}_x^2 &= \hat{\delta}_x^+ \hat{\delta}_x^- = 2 \cos \alpha - 2 \end{aligned}$$

where $-\pi \leq \alpha \leq \pi$ and $i^2 = -1$. Therefore, for the forward difference operator δ_x^+ , the real and imaginary parts of the symbol of the operator are $K_r = \cos \alpha - 1$ and $K_i = \sin \alpha$, respectively. Similarly, for the backward difference operator δ_x^- , $K_r = 1 - \cos \alpha$, $K_i = \sin \alpha$ and for the central difference operator δ_x^0 , $K_r \equiv 0$ and $K_i = \sin \alpha$.

In this paper an upwind compact operator is employed for the space derivative and formulated symbolically as

$$\delta_x^{c,\varepsilon} := (I - 2\varepsilon\delta_x^0 + \frac{1}{6}\delta_x^2)^{-1}(\delta_x^0 - 2\varepsilon\delta_x^2) \quad (4)$$

and the real and imaginary parts are, respectively, given by

$$K_r = \frac{\frac{2}{3}(\cos \alpha - 1)^2 \varepsilon}{\frac{1}{9} \cos^2 \alpha + \frac{4}{9} \cos \alpha + \frac{4}{9} + 4\varepsilon^2 \sin^2 \alpha} \quad (-\pi \leq \alpha \leq \pi) \quad (5)$$

$$K_i = \frac{8\varepsilon^2 \sin \alpha - 8\varepsilon^2 \sin \alpha \cos \alpha + \frac{1}{3} \sin \alpha \cos \alpha + \frac{2}{3} \sin \alpha}{\frac{1}{9} \cos^2 \alpha + \frac{4}{9} \cos \alpha + \frac{4}{9} + 4\varepsilon^2 \sin^2 \alpha} \quad (-\pi \leq \alpha \leq \pi) \quad (6)$$

where $a \cdot \varepsilon \geq 0$ and $-\frac{1}{3} < \varepsilon < \frac{1}{3}$. If $\varepsilon \neq 0$, it achieves third-order accuracy, whereas it can achieve fourth-order accuracy when $\varepsilon = 0$.

2.2. Numerical stability

The upwind compact difference operators $\delta_x^{c,\varepsilon}$ with control coefficient ε are used for discretizing the space derivative in Equation (1), the third-order Runge–Kutta method is used for approximating the time derivative. Equation (2) can then be rewritten as

$$\frac{\partial v}{\partial t} = L_h(v) \quad (7)$$

where L_h is the spatial difference operator, which is a third-order upwind compact difference operator. The third-order Runge–Kutta method can be expressed as

$$\begin{aligned} v^{(1)} &= \alpha_1 v^n + \beta_1 \Delta t L_h(v^n) \\ v^{(2)} &= \alpha_2 v^n + \beta_2 [v^{(1)} + \Delta t L_h(v^{(1)})] \\ v^{(n+1)} &= \alpha_3 v^n + \beta_3 [v^{(2)} + \Delta t L_h(v^{(2)})] \end{aligned} \quad (8)$$

with $\alpha_1 = 1, \alpha_2 = \frac{3}{4}, \alpha_3 = \frac{1}{3}, \beta_1 = 1, \beta_2 = \frac{1}{4}, \beta_3 = \frac{2}{3}$ and Neumann stability analysis is used to determine the stability limit. The numerical solution can be represented by a Fourier series, and for linear stability, substituting $v_j^n = G^n \exp(ikj\Delta x)$ into Equation (8), the amplification factor G for the third-order Runge–Kutta method can be obtained as

$$G = 1 - \lambda k_e + \frac{1}{2} \lambda^2 k_e^2 - \frac{1}{6} \lambda^3 k_e^3 \quad (9)$$

where $\lambda = a(\Delta t/\Delta x)$ is the Courant number, and

$$k_e = \frac{(\frac{1}{2} - 2\varepsilon)(\cos \alpha + i \sin \alpha) + 4\varepsilon - (\frac{1}{2} + 2\varepsilon)(\cos \alpha - i \sin \alpha)}{(\frac{1}{6} - \varepsilon)(\cos \alpha + i \sin \alpha) + \frac{2}{3} + (\frac{1}{6} + \varepsilon)(\cos \alpha - i \sin \alpha)} \quad (-\pi \leq \alpha \leq \pi) \quad (10)$$

is the Fourier symbol of the upwind compact difference operator $\delta_x^{c,\varepsilon}$.

For $|G| \leq 1$, we can obtain the relationship between λ_{\max} and ε . Figure 1(a) shows the distribution of the amplification factor against α , where $\varepsilon = \frac{1}{6}$. The reason for choosing $\varepsilon = \frac{1}{6}$ is explained in the next section. Figure 1(b) shows the distribution of λ_{\max} against ε . If a first-order explicit method is used for the approximation of time derivative, we may obtain

$$G = \frac{\frac{2}{3} + \frac{1}{3} \cos \alpha + 4\varepsilon \lambda (\cos \alpha - 1) - i(\lambda + 2\varepsilon) \sin \alpha}{\frac{2}{3} + \frac{1}{3} \cos \alpha - 2\varepsilon i \sin \alpha} \quad (11)$$

For $|G| \leq 1$, we have

$$\lambda \leq \min \left[\frac{8\varepsilon(\frac{2}{3} + \frac{1}{3} \cos \alpha)(1 - \cos \alpha) - 4\varepsilon \sin^2 \alpha}{16\varepsilon^2 + \sin^2 \alpha} \right] \quad (12)$$

As $\lambda = 0$, the first-order explicit method is unstable.

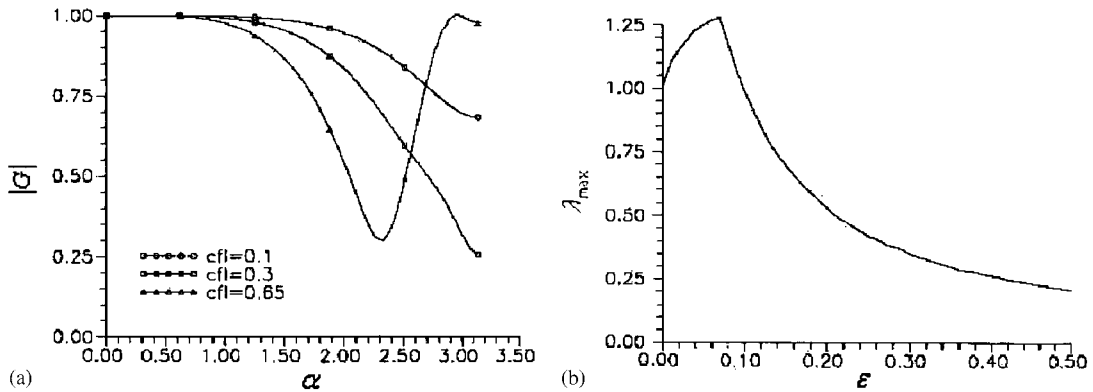


Figure 1. Distribution of $|G|$ and λ_{max} against ϵ : (a) distribution of $|G|$; and (b) distribution of λ_{max} .

2.3. Anisotropic effect

In multi-dimensional problems the dispersion effect appears in the form of anisotropy. Consider the two-dimensional unsteady advection of scalar u with constant velocity a and b , given by

$$\frac{\partial u}{\partial t} + a \frac{\partial u}{\partial x} + b \frac{\partial u}{\partial y} = 0 \tag{13}$$

with initial condition $u(x, y, 0) = \exp\{i(\mathbf{K} \cdot \mathbf{X})\}$, where $\mathbf{K} = [k_1, k_2]^T$ and $\mathbf{X} = [x, y]^T$, k_1, k_2 are wave numbers in the x and y directions, respectively. Defining

$$\mathbf{l} = \left[\frac{a}{\sqrt{a^2 + b^2}}, \frac{b}{\sqrt{a^2 + b^2}} \right]^T \tag{14}$$

it can be rewritten as $\mathbf{l} = [\cos \theta, \sin \theta]^T$, where θ is the azimuthal angle. The exact solution for Equation (13) with the initial condition can be expressed as

$$u(\mathbf{X}, t) = \exp\{i[\mathbf{K} \cdot \mathbf{X} - \sqrt{a^2 + b^2} \mathbf{K} \cdot \mathbf{l}t]\} \tag{15}$$

The semi-discrete approximation for Equation (13) is thus

$$\frac{\partial u_{ij}}{\partial t} + a \frac{\delta_x u_{ij}}{\Delta x} + b \frac{\delta_y u_{ij}}{\Delta y} = 0 \tag{16}$$

with initial condition $u(x, y, 0) = \exp\{i(\mathbf{K} \cdot \mathbf{X})\}$, where $\delta_x u_{ij}/\Delta x, \delta_y u_{ij}/\Delta y$ are approximations of the first derivatives $\partial u/\partial x, \partial u/\partial y$, respectively. The exact solution can be expressed as

$$u(\mathbf{X}, t) = \exp\{-\sqrt{a^2 + b^2} \mathbf{K} \cdot \mathbf{l}_r t\} \cdot \exp\{i\mathbf{K} \cdot [\mathbf{X} - \sqrt{a^2 + b^2} \mathbf{l}_i t]\} \tag{17}$$

Hence,

$$\mathbf{l}_r = \left[\cos \theta \frac{K_r^{(1)}}{\alpha}, \sin \theta \frac{K_r^{(2)}}{\beta} \right]^T, \quad \mathbf{l}_i = \left[\cos \theta \frac{K_i^{(1)}}{\alpha}, \sin \theta \frac{K_i^{(2)}}{\beta} \right]^T, \quad \alpha = k_1 \Delta x, \quad \beta = k_2 \Delta y$$

where $K_r^{(1)}, K_r^{(2)}, K_i^{(1)}, K_i^{(2)}, \mathbf{I}_r$ and \mathbf{I}_i are functions of α and β . In fact K_r and K_i are the real and imaginary parts of the symbols of difference operators, respectively. Consider the projection of numerical vectors \mathbf{I}_r and \mathbf{I}_i on \mathbf{I} , we have

$$\frac{\mathbf{I} \cdot \mathbf{I}_i}{\|\mathbf{I}\|} = \frac{1}{\omega} [\cos \theta K_i^{(1)} + \sin \theta K_i^{(2)}] \quad (0 \leq \theta \leq 2\pi) \quad (18)$$

where $K_i^{(1)} = K_i^{(1)}(\alpha), K_i^{(2)} = K_i^{(2)}(\beta)$ with $\alpha = \omega \cos \theta, \beta = \omega \sin \theta$. The upwind compact difference operator $\delta_x^{c,\varepsilon}$ with control coefficient ε is used for discretizing the space derivative in Equation (13). To obtain an optimal value of ε , consider the minimization problem:

$$\min_{\varepsilon} \int_0^{2\pi} \int_0^{2\pi} \left(\|\mathbf{I}\| - \frac{\mathbf{I} \cdot \mathbf{I}_i}{\|\mathbf{I}\|} \right)^2 d\theta d\omega$$

The computed results of Equation (18) with $\omega_m = m\pi/10, m = 0, 1, 2, \dots, 9$ for different values of ε are shown in Figure 2. It can be seen that the upwind compact operators with different coefficients ε have different anisotropic effect for high wave numbers. While the coefficient ε is increased, the anisotropic effect for the high wave numbers is alleviated. However, when ε is above a critical value, the anisotropic effect for high wave numbers is increased, indicating that there is an optimal value ε_{opt} and the range of wave numbers with small anisotropic effect is increased. In considering computational efficiency, ε_{opt} is approximately equal to $\frac{1}{6}$.

3. GOVERNING EQUATIONS OF THE PREMIXED V-FLAME

The main assumptions are as follows:

- (1) The flow is two-dimensional.
- (2) The flow is regarded as incompressible on either side of the flame due to low Mach number.
- (3) Vorticity is produced by baroclinic torque through the interaction of density gradients and pressure gradients.

The velocity field for the combustion process at low Mach number can be decomposed into three components

$$\mathbf{U} = \mathbf{U}_s + \mathbf{U}_v + \mathbf{U}_p \quad (19)$$

with the individual components satisfying the following conditions:

$$\nabla \cdot \mathbf{U}_s = \dot{m} \delta(\mathbf{x} - \mathbf{x}_f); \quad \nabla \times \mathbf{U}_s = 0 \quad (20)$$

$$\nabla \times \mathbf{U}_v = \omega(\mathbf{x}); \quad \nabla \cdot \mathbf{U}_v = 0 \quad (21)$$

$$\mathbf{U}_p = \nabla \phi; \quad \nabla \cdot \mathbf{U}_p = 0 \quad (22)$$

where \mathbf{U}_s is the velocity field due to volume expansion across the flame front, \mathbf{U}_v is the rotational velocity field due to vorticity, \mathbf{U}_p is the potential velocity field, the ratio of gas expansion is $\gamma = (\rho_u - \rho_b)/\rho_u$, ρ_u and ρ_b are gas densities of the unburnt and burnt mixtures, S_u

is the relative flame speed with respect to the unburnt side, x_f is the position vector of the flame front, and $\delta(\cdot)$ is the two-dimensional Dirac delta function. This is a Poisson equation with a singular volume source confined to the flame surface. Based on this equation, the irrotational part of the velocity field can be derived. The volume source $\dot{m} = S_b - S_u = [\gamma/(1-\gamma)]S_u$ is the net volume flux generated in the burnt products and consumed in the reactants.

The flame propagation is described by a scalar field $\psi(x, y, t)$ such that $\psi > 0$ in the unburnt region, $\psi < 0$ in the burnt region and $\psi = 0$ at the flame front. As the flame propagates with a burning speed S_u , the equation of flame propagation without advection is given by

$$\frac{\partial \psi}{\partial t} + S_u |\nabla \psi| = 0 \quad (23)$$

It is also advected by the accompanying flow field and the field equation becomes

$$\frac{\partial \psi}{\partial t} + \mathbf{U} \cdot \nabla \psi + S_u |\nabla \psi| = 0 \quad (24)$$

where \mathbf{U} is the convection velocity of the unburnt side. Following the idea of Markstein [18], the laminar burning speed for weak curvature is given by

$$S_u = S_u^0 (1 - \eta \kappa) \quad (25)$$

where S_u^0 is the laminar burning speed of a planar flame, $\kappa = -\nabla \cdot \mathbf{n}$ is the local curvature of flame front, and η is the Markstein length scale.

The distribution of vorticity is described by the Navier–Stokes equations in the form of

$$\frac{\partial \omega}{\partial t} + (\mathbf{U} \cdot \nabla) \omega = \frac{1}{Re} \nabla^2 \omega \quad (26)$$

The baroclinic torque term is a source of vorticity through the interaction of density gradients and pressure gradients. Pressure gradients tangential to the flame cause different accelerations in the unburnt and burnt sides with different densities and hence vorticity is produced at the flame front by the mean density gradient across the flame and the pressure gradient tangential to the flame. Based on Hayes [19], the vorticity jump $[\omega]$ across the flame front can be determined as

$$[\omega] = \left(\frac{1}{\rho_b} - \frac{1}{\rho_u} \right) \nabla_s (\rho_s S_u) - \frac{\rho_b - \rho_s}{\rho_u S_u} \left[\frac{dU_t}{d\tau} + U_t (\nabla_t U_t - V_n \kappa) - V_n \frac{\partial V_n}{\partial \tau} \right] \quad (27)$$

where U_t is the flow velocity at the flame front in the tangential direction of the flame front, ∇_t is its gradient along the flame front, V_n is the absolute normal flame speed, and $d/d\tau$ denotes the time derivative taken at a point on the front moving in the direction normal to the discontinuity.

4. NUMERICAL METHOD

4.1. Flame propagation

In this paper, an explicit method is presented to track the flame front. The equation for flame propagation is given by the Hamilton–Jacobi Equation (23) with initial condition

$$\psi(x, y, t = 0) = \pm d(x, y) \quad (28)$$

where d is the minimum distance from the point (x, y) to the flame front and the \pm sign is chosen for the unburnt/burnt region in the computational domain. The semi-discrete form of Equation (23) can be rewritten as

$$\frac{d\psi_{ij}}{dt} = -S_u^0(1 - \eta\kappa)f\{[(\max(\Delta x^{-1} \cdot \delta_x^{c,1/6}\psi_{ij}, 0))^2 + (\min(\Delta x^{-1} \cdot \delta_x^{c,-1/6}\psi_{ij}, 0))^2], \\ [(\max(\Delta y^{-1} \cdot \delta_y^{c,1/6}\psi_{ij}, 0))^2 + (\min(\Delta y^{-1} \cdot \delta_y^{c,-1/6}\psi_{ij}, 0))^2]\} \quad (29a)$$

where $f(a, b) = (a + b)^{1/2}$. The third-order accurate upwind compact difference operator with group velocity control is employed to approximate the advection part such that

$$\mathbf{U} \cdot \nabla \psi \approx -\frac{U_{ij}^+}{\Delta x} \delta_x^{c,1/6} \psi_{ij} - \frac{U_{ij}^-}{\Delta x} \delta_x^{c,-1/6} \psi_{ij} - \frac{V_{ij}^+}{\Delta y} \delta_y^{c,1/6} \psi_{ij} - \frac{V_{ij}^-}{\Delta y} \delta_y^{c,-1/6} \psi_{ij} \\ + \frac{1}{\Delta x} \sigma \delta_x^0 [\varphi_x(\psi_{ij}) ss_x(\psi_{ij}) \delta_x^2 \psi_{ij}] - \frac{1}{2\Delta x} \sigma \delta_x^2 [\varphi_x(\psi_{ij}) \delta_x^2 \psi_{ij}] \\ + \frac{1}{\Delta y} \sigma \delta_y^0 [\varphi_y(\psi_{ij}) ss_y(\psi_{ij}) \delta_y^2 \psi_{ij}] - \frac{1}{2\Delta y} \sigma \delta_y^2 [\varphi_y(\psi_{ij}) \delta_y^2 \psi_{ij}] \quad (29b)$$

where $\sigma \sim O(1)$, $ss_x = \text{sgn}(\delta_x^0 \psi_{ij} \cdot \delta_x^2 \psi_{ij})$, $ss_y = \text{sgn}(\delta_y^0 \psi_{ij} \cdot \delta_y^2 \psi_{ij})$ and $U_{i,j}^\pm = U_{i,j} \pm |U_{i,j}|/2$, $V_{i,j}^\pm = V_{i,j} \pm |V_{i,j}|/2$. The last two terms are group velocity control terms to eliminate numerical oscillations in the solution. $\delta_x^{c,\pm(1/6)}$, $\delta_y^{c,\pm(1/6)}$ are upwind compact difference operators satisfying the relations,

$$\frac{2}{3} \delta_x^{c,1/6} \psi_{ij} + \frac{1}{3} \delta_x^{c,1/6} \psi_{i-1,j} = \frac{1}{6} \psi_{i+1,j} + \frac{2}{3} \psi_{ij} - \frac{5}{6} \psi_{i-1,j} \quad (i = 1, 2, \dots, I-1) \quad (30a) \\ \frac{1}{3} \delta_x^{c,-1/6} \psi_{i+1,j} + \frac{2}{3} \delta_x^{c,-1/6} \psi_{ij} = \frac{5}{6} \psi_{i+1,j} - \frac{2}{3} \psi_{ij} - \frac{1}{6} \psi_{i-1,j}$$

$$\frac{2}{3} \delta_y^{c,1/6} \psi_{ij} + \frac{1}{3} \delta_y^{c,1/6} \psi_{i,j-1} = \frac{1}{6} \psi_{i,j+1} + \frac{2}{3} \psi_{ij} - \frac{5}{6} \psi_{i,j-1} \quad (j = 1, 2, \dots, J-1) \quad (30b) \\ \frac{1}{3} \delta_y^{c,-1/6} \psi_{i,j+1} + \frac{2}{3} \delta_y^{c,-1/6} \psi_{ij} = \frac{5}{6} \psi_{i,j+1} - \frac{2}{3} \psi_{ij} - \frac{1}{6} \psi_{i,j-1}$$

At the boundary, the second-order accurate one-side difference approximations are used such that

$$\delta_x^{c,1/6} \psi_{0,j} = (-3\psi_{0,j} + 4\psi_{1,j} - \psi_{2,j})/2, \quad \delta_x^{c,-1/6} \psi_{I,j} = (3\psi_{I,j} - 4\psi_{I-1,j} + \psi_{I-2,j})/2 \quad (31) \\ \delta_y^{c,1/6} \psi_{i,0} = (-3\psi_{i,0} + 4\psi_{i,1} - \psi_{i,2})/2, \quad \delta_y^{c,-1/6} \psi_{i,J} = (3\psi_{i,J} - 4\psi_{i,J-1} + \psi_{i,J-2})/2$$

and $\delta_x^{c,\pm(1/6)} \psi_{ij}$, $\delta_y^{c,\pm(1/6)} \psi_{ij}$ can be obtained by the alternating direction sweeping method.

To avoid spurious oscillations while maintaining accuracy of the scheme, a switching function ‘ φ_j ’ given by Swanson [20], is used

$$\varphi_x(\psi_{i,j}) = \begin{cases} 1, & \frac{|\psi_{i+1,j} - 2\psi_{i,j} + \psi_{i-1,j}|}{0.5(|\psi_{i+1,j} - \psi_{i,j}| + |\psi_{i,j} - \psi_{i-1,j}|) + 0.5|\psi_{i+1,j} + 2\psi_{i,j} + \psi_{i-1,j}|} \geq C \\ 0, & \frac{|\psi_{i+1,j} - 2\psi_{i,j} + \psi_{i-1,j}|}{0.5(|\psi_{i+1,j} - \psi_{i,j}| + |\psi_{i,j} - \psi_{i-1,j}|) + 0.5|\psi_{i+1,j} + 2\psi_{i,j} + \psi_{i-1,j}|} < C \end{cases} \quad (32)$$

where C is a threshold, taken as 0.95 in this paper. Also, φ_x takes the values of 1 and 0 in the steep-and-smooth and smooth regions, respectively. The switching function guarantees that the scheme is of $O(\Delta x^3)$ in smooth regions.

4.2. Velocity field due to exothermicity

Based on the Ψ -field, the updated location of the flame front can be determined by the contour of $\psi_{i,j}^n$ corresponding to $\psi=0$. The grid cells with four grid values of different signs were located and then bisected by the line separating the burnt region from that of the unburnt region. The position and length of each flame segment within these cells determine the position and strength of the volumetric source. The volumetric source of strength m in these grid cells containing the flame segments can be calculated by $m = [\gamma/(1-\gamma)]S_u\Delta L$, where ΔL is the length of the flame segment. It becomes the source term of the Poisson equation for the velocity potential due to exothermicity.

$$\nabla^2 \phi_{i,j} = q_{i,j} \quad (33)$$

where $q_{i,j}$ is the source term, $\phi_{i,j}$ can be obtained by using a standard Poisson solver on an Eulerian grid. The volume source of strength $m = [\gamma/(1-\gamma)]S_u\Delta L$ at the midpoint of the flame segment within a cell needs to be distributed to the nearest grid points with value $q_{i,j}$ using an area-weighting scheme. The corresponding velocity field can be calculated using central compact difference of $\phi_{i,j}$ and can be rewritten as

$$\begin{aligned} \frac{1}{6}u_{s,i+1,j} + \frac{2}{3}u_{s,i,j} + \frac{1}{6}u_{s,i-1,j} &= \frac{1}{\Delta x} \delta_x^0 \phi_{i,j} \\ \frac{1}{6}v_{s,i,j+1} + \frac{2}{3}v_{s,i,j} + \frac{1}{6}v_{s,i,j-1} &= \frac{1}{\Delta y} \delta_y^0 \phi_{i,j} \end{aligned} \quad (34)$$

As the open V-flame is unconfined, Neumann boundary condition is used to match the total volume generated inside the computational domain with the net outflow across the boundaries,

$$\iint_D \nabla^2 \phi \, dx \, dy = \iint_D q \, dx \, dy = \oint_{\partial D} \nabla \phi \cdot \mathbf{n} \, ds \quad (35)$$

4.3. Velocity field due to baroclinicity

The vorticity $\omega = \nabla \times \mathbf{U}_v$ is produced by the baroclinic torque term $-\nabla(1/\rho) \times \nabla p$ in the vorticity transport equation. The vorticity jump $[\omega]$ across the flame front can be determined

by Hayes's formulation [19]. Flame-induced vortices are injected on the burnt side at each time step such that $\omega_b = [\omega]$ with circulation $\Gamma_b = \omega_b S_b \Delta L \Delta t$. The area of each blob is given by $\Delta A = S_b \Delta L \Delta t$ which is equivalent to a vortex blob sweeping out an area of length ΔL and width $S_b \Delta t$. Assuming the blob to be circular, its radius is simply defined as $c = \sqrt{\Delta A / \pi}$.

The vorticity field in the computational domain forms the source term in the Poisson equation for the vorticity stream function $\Psi_{i,j}$ such that

$$\nabla^2 \Psi_{i,j} = -\omega_{i,j} \quad (36)$$

where $\omega_{i,j}$ at cell corners on an Eulerian grid are evaluated again by distributing the circulation within each cell using the area weighting method.

Neumann boundary condition is employed such that the negative of the total circulation inside the domain is equal to the contour integral of the normal derivative of the boundaries of the stream function. The corresponding velocity field can be solved using the central compact difference approximation of $\Psi_{i,j}$.

$$\begin{aligned} \frac{1}{6}v_{v,i+1,j} + \frac{2}{3}v_{v,i,j} + \frac{1}{6}v_{v,i-1,j} &= -\frac{1}{\Delta x} \delta_x^0 \Psi_{i,j} \\ \frac{1}{6}u_{v,i,j+1} + \frac{2}{3}u_{v,i,j} + \frac{1}{6}u_{v,i,j-1} &= \frac{1}{\Delta y} \delta_y^0 \Psi_{i,j} \end{aligned} \quad (37)$$

The combination of rotational velocity together with the irrotational velocity due to exothermicity and the uniform potential velocity yield the total velocity that moves the flame by advection.

4.4. Vortex motion

The distribution of vorticity, which is described by the Navier–Stokes equations, can be decomposed by means of a fractional step method as

$$\frac{\partial \omega}{\partial t} + (\mathbf{U} \cdot \nabla) \omega = 0 \quad (38a)$$

and

$$\frac{\partial \omega}{\partial t} = \frac{1}{Re} \nabla^2 \omega \quad (38b)$$

The vortex blobs moving with local fluid velocities can be calculated using the third-order Runge–Kutta method. Solution to Equation (38b) is obtained by Chorin's random vortex method in which the diffusion process during each time step Δt is modelled as a random walk with a Gaussian distribution of zero mean and standard deviation $(2\Delta t/Re)^{1/2}$.

In order to avoid blowout, the flame is numerically anchored at a fixed point. The flame is held at the flame holder by placing an initial ignition ψ_{th} field on a grid at the location of the flame holder and allowing ψ_{th} to act as a source of ignition impulse. As the flame front moves with the accompanying flow field, it is continuously re-ignited at the location of the flame holder by superimposing ψ_{th} onto the existing ψ .

5. NUMERICAL EXAMPLES FOR MODEL EQUATIONS

To investigate the behaviour of the method, the following examples are considered.

Example 1

Consider the two-dimensional linear conservation law with variable coefficients

$$u_t + (-yu)_x + (xu)_y = 0, \quad -1 \leq x, y \leq 1 \quad (39)$$

with periodic boundary conditions. The initial condition is chosen such that

$$u(x, y, 0) = \begin{cases} a; & \sqrt{x^2 + y^2} \leq 0.5 \\ b; & \sqrt{x^2 + y^2} > 0.5 \end{cases} \quad (40)$$

where a and b are constants. The initial condition therefore corresponds to a characteristic function on a circle of rotation with radius 0.5. Figure 3 shows the results at $t = 0.8$, using 200×200 points. The initial values inside and outside the circle are denoted in red and in blue, respectively. Third-order Runge–Kutta time discretization with central compact difference approximation ($\varepsilon = 0.0$) is employed to discretize the spatial derivatives, and is shown in Figure 3(a). The numerical oscillations are obvious particularly around the circumference of the circle, and some degree of effects of anisotropy is found. Figure 3(b) shows that numerical solutions using the third-order upwind compact difference scheme, with a control coefficient $\varepsilon = 0.1$ is improved. However, some oscillations in the numerical solutions still exist inside the circle. Figure 3(c) shows the results when $\varepsilon = \frac{1}{6}$ is used in the upwind compact difference scheme. It can be seen that oscillations are very slight and the solutions are much more satisfactory. Therefore, in this paper, an optimal value of control coefficient in the upwind compact difference scheme is chosen as $\varepsilon_{\text{opt}} = \frac{1}{6}$.

Example 2

Consider the equation

$$u_t - c\sqrt{1 + u_x^2} = 0 \quad (41a)$$

Given continuous initial data, it is well-known that the above equation corresponds to motion with constant normal velocity c . The corresponding level set equation is given by

$$\phi_t + c|\nabla\phi| = 0 \quad (41b)$$

which describes constant normal speed of each level set of ϕ . The above equation is evaluated using the method in Equation (29a), where $\varepsilon_{\text{opt}} = \frac{1}{6}$. Figure 4 shows the zero level curves of ϕ in different times at $t = 0, 0.2, 0.4$ and 0.6 . It can be seen that each curve is equidistant from the original curve, shown in red.

6. NUMERICAL SIMULATION OF THE PREMIXED V-FLAME

In this paper, numerical simulation of a premixed V-flame is carried out using the upwind compact difference scheme with an optimal value of control coefficient ε_{opt} . In order

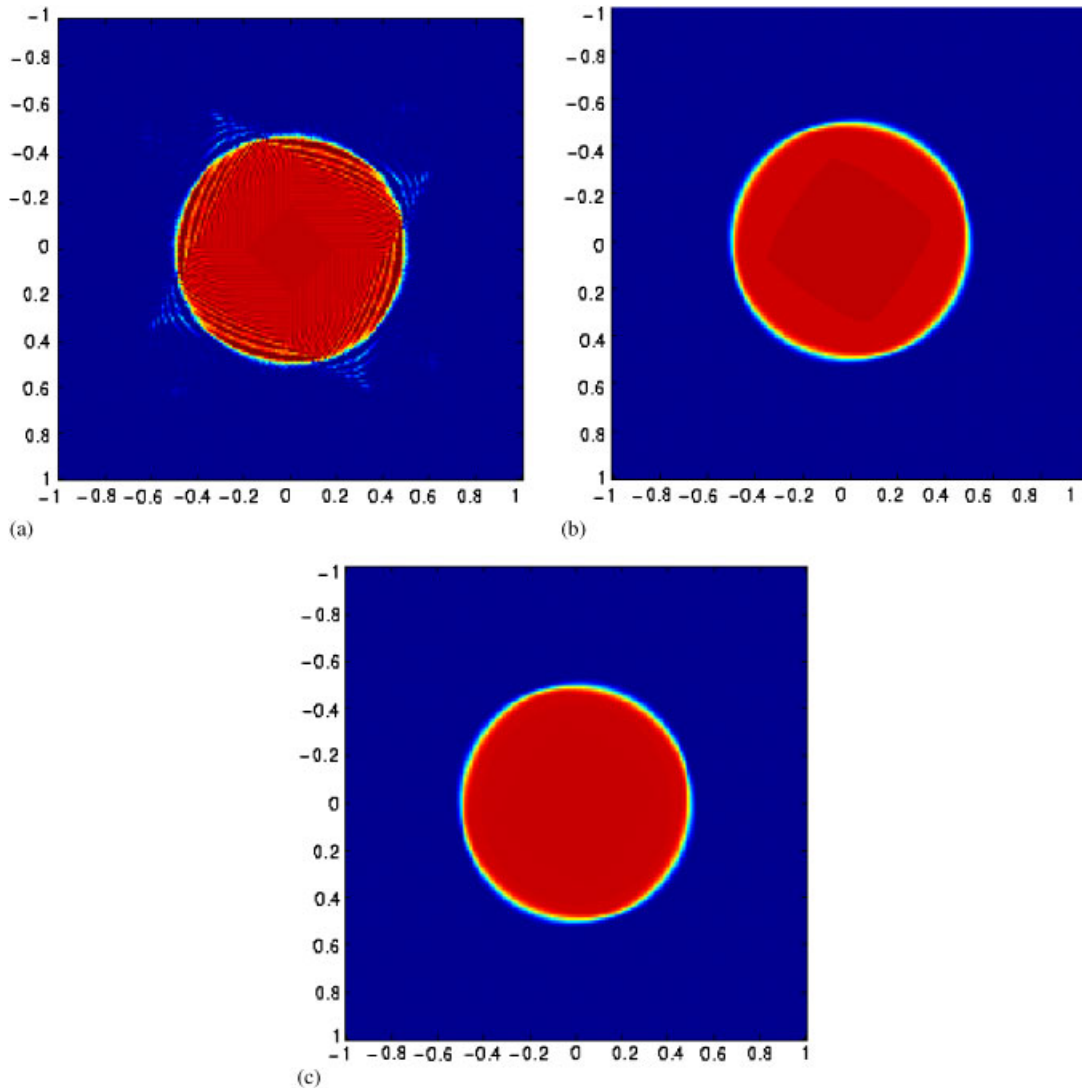


Figure 3. (a) Central compact difference scheme with $\varepsilon = 0.0$; (b) third-order upwind compact difference scheme with $\varepsilon = 0.1$; and (c) third-order upwind compact difference scheme with $\varepsilon = \frac{1}{6}$.

to compare with experimental data available, conditions of the experiments of Cheng *et al.* [6–8] are used. A schematic diagram of the experimental set-up is shown in Figure 5. Parameters used are inflow velocity $U_0 = 5.5 \text{ m s}^{-1}$, equivalence ratio $\Phi = 0.7$ for $\text{C}_2\text{H}_4/\text{air}$, laminar burning speed $S_b = 0.44 \text{ m s}^{-1}$, Markstein length scale $\eta = 10^{-3} \text{ m}$ and Reynolds number $Re = 2.8 \times 10^4$, where the characteristic length in defining Re is taken as 50 mm, which is the diameter of the inner coaxial cylinder. The computational domain is taken as

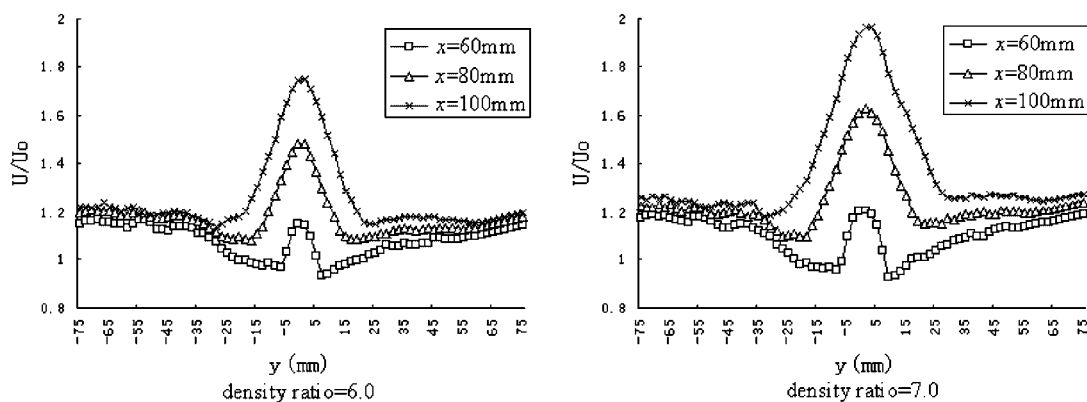


Figure 6. Distribution of mean axial velocity.

150 × 150 mm², with a grid system of 151 × 151 nodes. Based on Courant condition of stability, the nondimensional time step is chosen as 0.004. Free-stream turbulence is incorporated into the computation domain by injecting vortices of equal size and strength at 50 mm upstream of the flame holder. The vortices are injected at random positions in the interval between $y = \pm 50$ mm. Equal numbers of positive and negative vortices are injected at each injection. Vortices of radius 1 mm and nondimensional circulation $\Gamma = 0.01$ are used in our computation. In this paper, 48 vortices are injected for every 12 time steps. The statistic results are obtained by averaging the instantaneous values over 2000 time steps.

In order to demonstrate the performance of this method and reveal some of the mechanisms of gas expansion on the flow field, different density ratios are simulated. Figure 6 shows the axial velocity distributions at different upstream positions. The flame holder is located at $x = 50$ mm. It can be seen that the flow is accelerated across the flame front and higher density ratio increases the velocity more significantly. Also, the velocity is at a peak near the central axis. The distributions of mean transverse velocity from $x = 60$ mm to $x = 110$ mm are shown in Figure 7. Similar to the axial velocity distribution, higher density ratio also causes an increase in V .

The distribution of fluctuating velocities upstream of the flame holder at $x = 25$ mm, computed from the mean and instantaneous values, is shown in Figure 8. It can be seen that free-stream turbulence is nearly isotropic, with average level of about 10%, showing reasonable agreement with Cheng's experimental observations.

By means of an intermittency factor Ω , the Eulerian-averaged (unconditioned) mean velocity can be defined as

$$\begin{aligned} U &= (1 - \Omega)U_r + (\Omega)U_p \\ V &= (1 - \Omega)V_r + (\Omega)V_p \end{aligned} \quad (42)$$

where subscripts r and p correspond to conditioned mean velocities in the reactants and in the products, respectively. Ω represents the probability of the products, which varies from 0.0 in the reactants to 1.0 in the products across the flame brush. Similar definition for fluctuating velocities can also be obtained. Ω can be obtained by sampling the time record of a variable

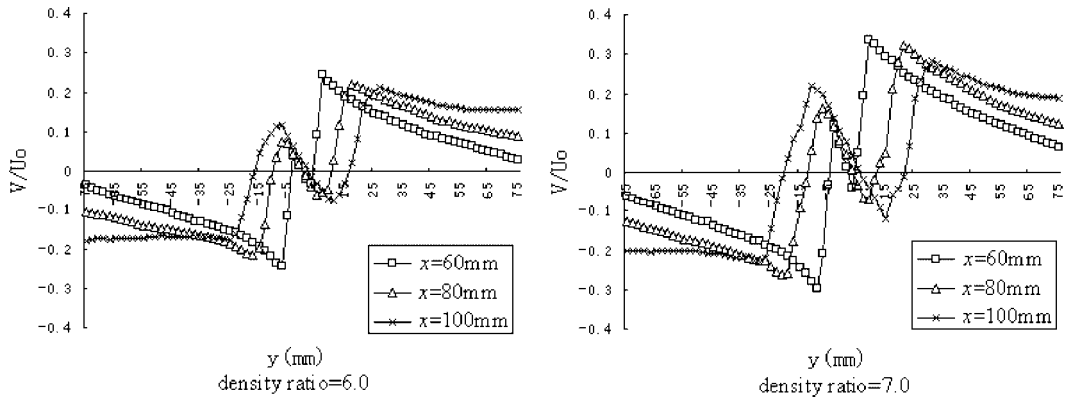
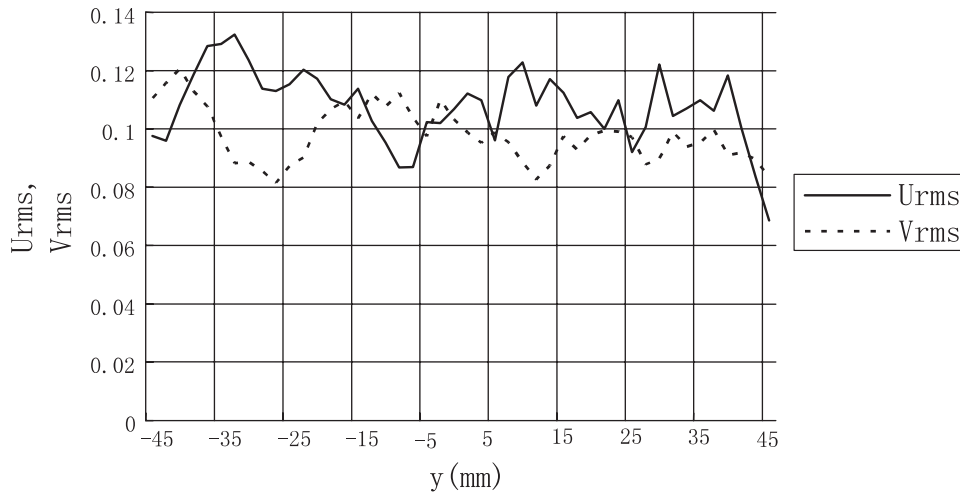


Figure 7. Distribution of mean transverse velocity.

Figure 8. Distribution of fluctuating velocities U_{rms} and V_{rms} at $x = 25$ mm.

and evaluating N_p/N_t where N_p is the number of samples associated with product and N_t is the total number of samples. Figure 9 shows the distribution of the intermittency factor at $x = 100$ mm. It can be seen that the numerical solutions using the upwind compact difference scheme with the optimal value of control coefficient of $\frac{1}{6}$ are comparable to experimental measurements.

The unconditional axial and transverse fluctuating velocity profiles at $x = 100$ mm are shown in Figure 10. It can be seen that the fluctuating statistics is not very sensitive to the density ratio. The fluctuating velocity behind the flame front increases with the increase of x , while in the other regions the fluctuations remain at the free-stream level of about 10%. In turbulent premixed V-flame, the Favre correlation $\overline{u''c''}$ is determined by the two contributions to scalar transport: one due to turbulent mixing and the other due to gas expansion.

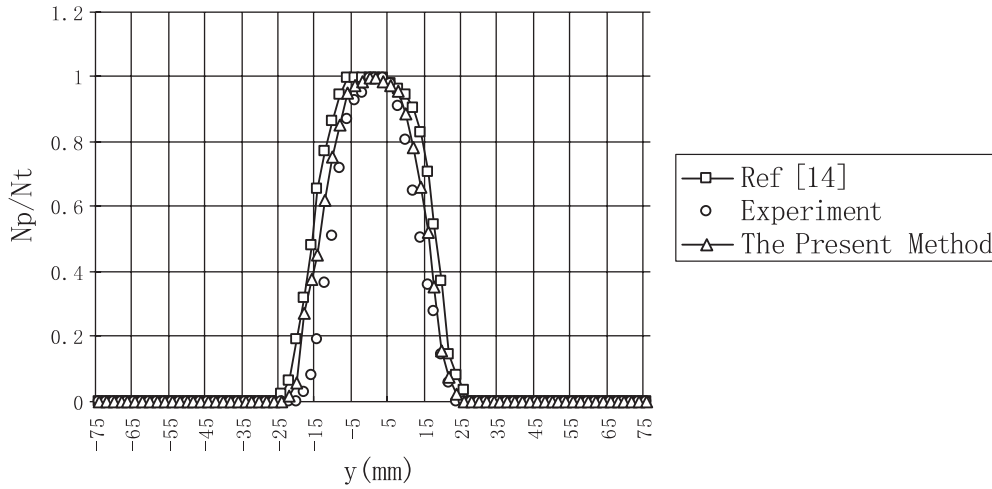


Figure 9. Distribution of intermittency factor at $x = 100$ mm.

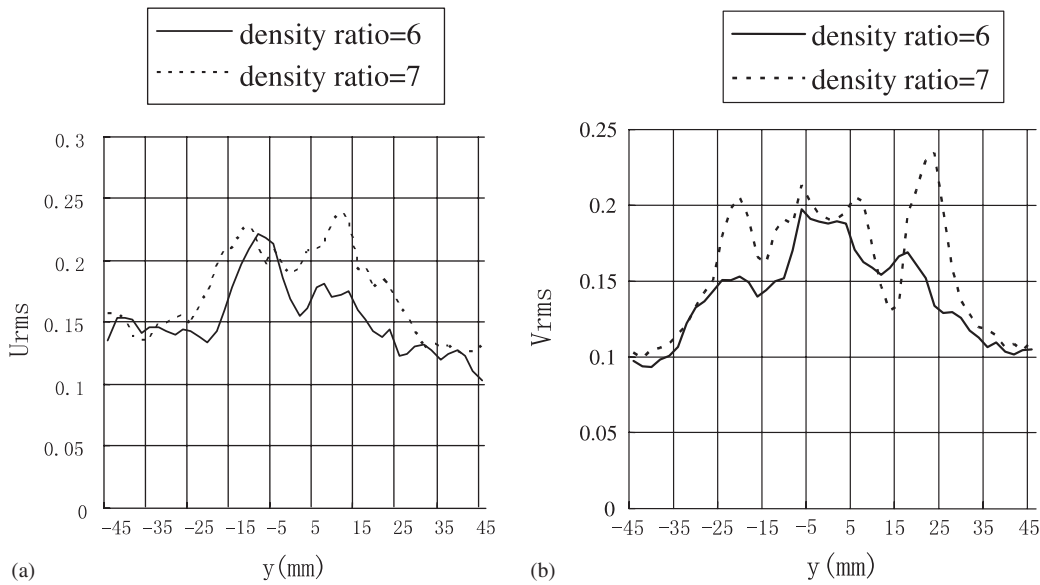


Figure 10. (a) Distribution of fluctuating velocity U_{rms} at $x = 100$ mm; and (b) distribution of fluctuating velocity V_{rms} at $x = 100$ mm.

The first term results in gradient diffusion and the second term in counter gradient diffusion. A simple model for $\overline{u''c''}$ was derived by Veynante *et al.* [21] as

$$\overline{u''c''} = \bar{c}(1 - \bar{c}) \left(\frac{\gamma}{1 - \gamma} S_L - 2\zeta v' \right) \tag{43}$$

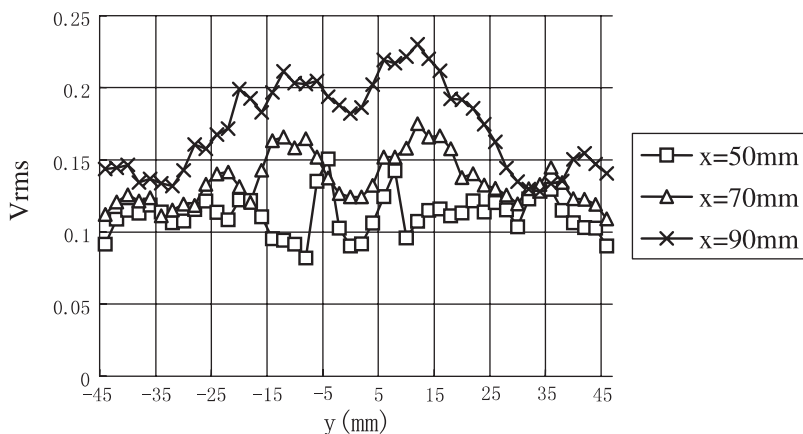


Figure 11. Distribution of fluctuating velocities.

where the modelling coefficient ζ is of order unity, c is the progress variable, viewed as a normalized product mass fraction, defined as $c = Y_c/Y_c^{\text{Eq}}$, with Y_c^{Eq} as the equilibrium condition of Y_c , and having a value of 1 in the fully burnt product region and 0 in the fresh reactant region. The Favre-averaged progress variable can be defined as $\bar{c} \equiv \overline{\rho c}/\bar{c}$. The sign of Equation (43) is determined by the ratio of gas expansion, the laminar burning speed and fluctuating velocity. It is clear that Equation (43) is capable of describing the transition from counter gradient diffusion to gradient diffusion when the ratio v'/S_L is increased. From Equation (43), counter gradient diffusion is observed when $[\gamma/(1-\gamma)]S_L - 2\zeta v' \geq 0$, or when $\gamma S_L/[2(1-\gamma)\zeta v'] \geq 1$, which is consistent with the Bray–Moss–Libby theory. Transition from counter gradient diffusion to gradient diffusion occurs when $\gamma S_L/[2(1-\gamma)\zeta v'] = 1$. Since the fluctuating statistics is not sensitive to density ratio, fluctuating velocities behind the flame front are similar for different density ratios.

Figure 11 shows that distribution of fluctuating velocities at different locations behind the flame holder for the case when density ratio is equal to 7. It can be seen that, close to the flame holder at $x \approx 55$ mm, $[\gamma/(1-\gamma)]S_L - 2\zeta v' \approx 2.52 > 0$, where $\zeta \approx 0.5$. In this region, the positive $\overline{u''c''}$ shows that counter gradient diffusion is dominant due to gas expansion. With the increase of x , transition from counter gradient diffusion to gradient diffusion occurs due to the increase of v' when $\gamma S_L/[2(1-\gamma)\zeta v'] = 1$. As larger gas expansion depends on higher fluctuating velocity, transition from counter gradient diffusion to gradient diffusion occurs at positions further downstream of the flame holder, due to turbulent mixing. It shows that the energy-containing eddies at the integral scale are strong enough to suppress local gas expansion and the effect of gas expansion are dominated by kinematic restoration.

Figure 12 shows an instantaneous flame configuration with the accompanying velocity field at $t = 12$. It can be seen that our results are comparable with results obtained by the conventional upwind difference scheme [14].

The distribution of flame brush thickness δ_t along the axial direction is shown in Figure 13. It can be seen that the numerical solutions obtained using the present method are better than those obtained previously [14] and compared well with experimental measurements.

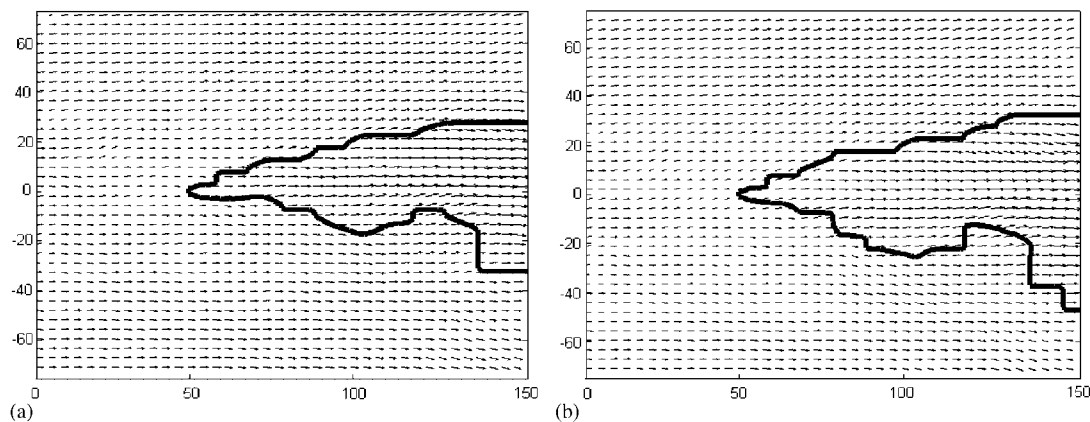


Figure 12. (a) Velocity field, with the upwind scheme; and (b) velocity field, with the upwind compact scheme.

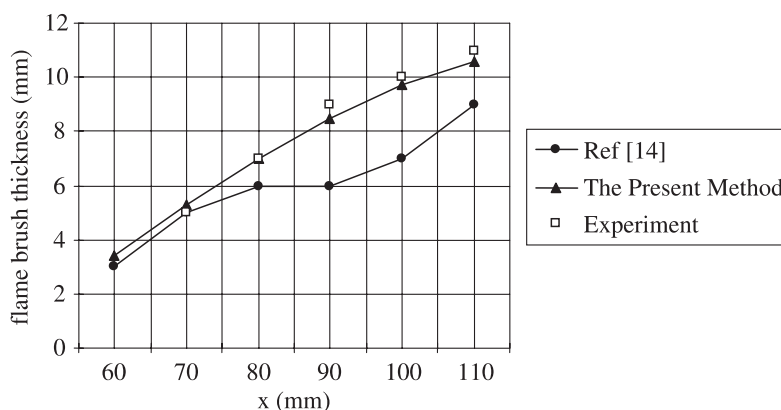


Figure 13. Flame brush thickness.

The reason of the discrepancy of the previous prediction is likely to be due to the overdissipative effects of the previous scheme.

7. CONCLUSIONS

In this paper, applicability of the newly developed upwind compact scheme to simulate the complex flow field in a premixed V-flame is considered. Compared with traditional difference schemes, upwind compact schemes have higher accuracy for the same stencil width. Additionally, the upwind compact finite difference scheme is an upwind-based scheme and is more suitable for simulation of complex flow fields due to its stability. In multi-dimensional problem, the effect of anisotropy in the upwind compact difference scheme is analysed and

obtained an optimal value of the control coefficient for this scheme. The scheme is of third-order accuracy in smooth regions. The scheme is combined with Runge–Kutta time discretization to simulate the turbulent premixed V-flame. Numerical results are found to be satisfactory and useful in tracking the flame front and interaction of different vortices.

ACKNOWLEDGEMENTS

This work was partially supported by the National Natural Science Foundation of China under Grant number 10102024 and the Research Grant Council of the Hong Kong SAR (Account Code PolyU 5246/03E and B-Q653).

REFERENCES

1. Zhu QY, Li Y. An upwind compact approach with group velocity control for compressible flow fields. *International Journal for Numerical Methods in Fluids* 2004; **44**:463–482.
2. Fu DX, Ma YW. A high order accurate finite difference scheme for complex flow fields. *Journal of Computational Physics* 1997; **134**:1–15.
3. Veynante D, Piana J, Duclos JM, Martel C. Experimental analysis of flame surface density models for premixed turbulent combustion. *Twenty-sixth International Symposium on Combustion*, Pittsburgh, PA. The Combustion Institute 1996; 413–420.
4. Alshaaan TM, Rutland CJ. Turbulence, scalar transport and reaction rates in flame-wall interaction. *Twenty-seventh International Symposium on Combustion*, Pittsburgh, PA. The Combustion Institute 1998; 793–799.
5. Galizzi C, Escudie D. Experimental study of a turbulent V-shaped flame stabilized in a stratified flow. *The Third International Symposium on Turbulence and Shear Flow Phenomena* 2003; 1007–1012.
6. Cheng RK. Conditional sampling of turbulence intensities and Reynolds stress in premixed turbulent flame. *Combustion Science and Technology* 1984; **41**:109–142.
7. Cheng RK, Shepherd IG. Interpretation of conditioned statistics in open oblique premixed turbulent flames. *Combustion Science and Technology* 1986; **49**:17–40.
8. Cheng RK, Talbot L, Robben F. Conditional velocity statistics in mixed CH₄-AIR and C₂H₄-AIR turbulent flames. *Twentieth International Symposium on Combustion*, Pittsburgh, PA. The Combustion Institute 1984; 453–461.
9. Tanahashi M, Miyauchi T, Ikeda J. Scaling law of coherent fine scale structure in homogenous turbulence. *Proceedings of the 11th Symposium on Turbulent Shear Flow*, Grenoble, vol. 1, 1997; 4–17.
10. Tanahashi M, Iwase S, Miyauchi T. Appearance and alignment with strain rate of coherent fine scale eddies in turbulent mixing layer. *Journal of Turbulence* 2001; **2**(6):1–17.
11. Baum M, Poinso TJ, Haworth DC, Darabiha N. Direct numerical simulation of H₂/O₂/N₂ flames with complex chemistry in two-dimensional turbulent flows. *Journal of Fluid Mechanics* 1994; **281**(1):1–32.
12. Pindera MZ, Talbot L. Some fluid dynamics considerations in the modeling of flames. *Combustion and Flames* 1988; **73**:111–125.
13. Rhee CW, Talbot L, Sethian JA. Dynamical behavior of a premixed turbulent open V-flame. *Journal of Fluid Mechanics* 1995; **300**:87–115.
14. Chan CK, Lau KS, Zhang BL. Simulation of a premixed turbulent flame with the discrete vortex method. *International Journal for Numerical Methods in Engineering* 2000; **48**:613–627.
15. Chorin AJ. Numerical study of slight viscous flow. *Journal of Fluid Mechanics* 1973; **57**:786–796.
16. Chan CK, Wang HY, Tang HY. Effect of intense turbulence on turbulent premixed V-flame. *International Journal of Engineering Science* 2003; **41**:903–916.
17. Shu CW. Total variation diminishing time discretizations. *SIAM Journal on Scientific and Statistical Computing* 1988; **9**:1073–1084.
18. Markstein GH. *Nonsteady Flame Propagation*. Pergamon Press: Oxford, 1964.
19. Hayes WD. The vorticity jump across a gas dynamic discontinuity. *Journal of Fluid Mechanics* 1959; **2**:595–600.
20. Swanson RC. On central-difference and upwind schemes. *Journal of Computational Physics* 1992; **101**:292–306.
21. Veynante D, Trouve A, Bray KNC, Mantel T. Gradient and counter-gradient scalar transport in turbulent premixed flames. *Journal of Fluid Mechanics* 1997; **332**:263–293.